

# Chaos of energetic positron orbits in a dipole magnetic field and its potential application to a new injection scheme

H. Saitoh,<sup>1,2</sup> Z. Yoshida,<sup>2</sup> Y. Yano,<sup>2</sup> M. Nishiura,<sup>2</sup> Y. Kawazura,<sup>2,\*</sup> J. Horn-Stanja,<sup>1</sup> and T. Sunn Pedersen<sup>1,3</sup>

<sup>1</sup>Max Planck Institute for Plasma Physics, Boltzmannstraße 2, D-85748 Garching and Wendelsteinstraße 1, D-17491 Greifswald, Germany

<sup>2</sup>Graduate School of Frontier Sciences, The University of Tokyo, 5-1-5 Kashiwanoha, Kashiwa, Chiba 277-8561, Japan

<sup>3</sup>Ernst Moritz-Arndt University Greifswald, Domstraße 11, 17489 Greifswald, Germany

(Received 12 May 2016; published 19 October 2016)

We study the behavior of high-energy positrons emitted from a radioactive source in a magnetospheric dipole field configuration. Because the conservation of the first and second adiabatic invariants is easily destroyed in a strongly inhomogeneous dipole field for high-energy charged particles, the positron orbits are nonintegrable, resulting in chaotic motions. In the geometry of a typical magnetospheric levitated dipole experiment, it is shown that a considerable ratio of positrons from a  $^{22}\text{Na}$  source, located at the edge of the confinement region, has chaotic long orbit lengths before annihilation. These particles make multiple toroidal circulations and form a hollow toroidal positron cloud. Experiments with a small  $^{22}\text{Na}$  source in the Ring Trap 1 (RT-1) device demonstrated the existence of such long-lived positrons in a dipole field. Such a chaotic behavior of high-energy particles is potentially applicable to the formation of a dense toroidal positron cloud in the strong-field region of the dipole field in future studies.

DOI: [10.1103/PhysRevE.94.043203](https://doi.org/10.1103/PhysRevE.94.043203)

## I. INTRODUCTION

Self-organization of charged particles in a strongly inhomogeneous dipole magnetic field [1,2] is a fundamental plasma phenomenon, which is widely observed in planetary and laboratory magnetospheres [3,4]. Recent experiments in dipole configurations [5,6] have demonstrated formation of a stable vortex structure of a non-neutral plasma [7] and particle acceleration [8] by the inward diffusion mechanism [9]. In the Ring Trap 1 (RT-1) device [10], long confinement ( $>300$  s) of an electron plasma has been realized [11]. As one of the toroidal geometries [12–17], the dipole configuration can trap plasmas at any degree of non-neutrality, which is applicable to the formation of electron-positron plasmas [18–21]. The electron-positron plasmas are predicted to exhibit unique wave and stability properties as one of pair-plasmas [22–24]. Experimentally, beam-plasma interaction of electrons and positrons [25], weakly ionized fullerene pair-plasma [26], and laser-based dense electron positron pairs [27] have been investigated. However, magnetically confined electron-positron plasmas have never been realized so far.

In order to confine charged particles in the dipole configuration, it is important to develop an efficient injection scheme for particles across closed field lines. This is especially the case for positrons, where the available beam current is by far smaller than that for electrons. Here use of a reactor-based intense positron source [28] is a promising approach for such a purpose [19,20]. Another common positron source is a radioactive isotope. Among positron-emitting isotopes,  $^{22}\text{Na}$  is a widely used one, which has the advantages of a relatively long half-life of 2.6 years, a high positron yield of 90.4%, and almost simultaneous emission of a 1.27-MeV  $\gamma$  ray with the positron. Positrons emitted from a  $^{22}\text{Na}$  source have a broad energy distribution with an end-point energy of 543 keV and

peaking at approximately 200 keV, because of a three-body decay. Many experiments, for example, in surface physics or in linear trapping configurations, require positrons of low kinetic energy. The high-energy positrons from the radioactive sources are therefore converted into a low-energy beam using a moderator [29]. In this study, however, we focus on the behavior of high-energy positrons emitted from a radioactive source and consider the possibility of their direct injection and trapping in a toroidal geometry.

Adiabatic invariants are key parameters to understand the behavior of charged particles in a dipole magnetic field [2,30]. There are three adiabatic invariants as actions for the associated periodic motions in a dipole field; magnetic moment  $\mu$  for a gyromotion, longitudinal invariant  $J$  for a vertical bounce motion, and magnetic flux  $\Psi$  for toroidal precession. When the three adiabatic invariants are conserved, injected positrons return to the source after short periodic motions and are lost before filling the confinement region. However, as theoretically and numerically studied in relation to particle motions in planetary magnetospheres [31,32], orbits of charged particles in a dipole field are often nonadiabatic. In general, only energy  $H$  and canonical angular momentum  $P_\theta \sim \Psi$  are the constants of motion in a static dipole field. Because there are two constants of motion for a system with three degrees of freedom, charged particle motions in a dipole field are nonintegrable in general and can be chaotic [2,30]. Thus breakdown of the invariants results in chaotic motions [33–35] of positrons, which enable long orbits and multiple toroidal rotations in the confinement region before annihilation. Once positrons are injected into such toroidally rotating orbits, it is possible to further transport them into a strong-field region by applying slow fluctuations. This is realized through the strong “inward diffusion” effects of the dipole field caused by the flattening of density distribution in the phase space [1,2,9]. Thus the chaotic behavior of orbits is potentially applicable to a new injection scheme of charged particles in the dipole field configuration. In the following sections, we report numerical studies on the chaotic behavior of high-energy positrons in a dipole field

\*Current address: Department of Physics, University of Oxford, UK.

(Sec. II) and preliminary experiments in RT-1 using a small  $^{22}\text{Na}$  source (Sec. III).

## II. ORBIT ANALYSIS OF POSITRONS IN A DIPOLE MAGNETIC FIELD

### A. Chaotic behavior of energetic positrons

We study the behavior of high-energy positrons in a dipole field by numerically integrating the equation of motion with the fourth-order Runge-Kutta method. In the electric and magnetic fields  $\mathbf{E}$  and  $\mathbf{B}$ , the relativistic equation of motion of a particle with a charge  $q$  and a mass  $m$  is

$$\frac{d}{dt}(\gamma m \mathbf{v}) = q(\mathbf{E} + \mathbf{v} \times \mathbf{B}), \quad (1)$$

where  $\gamma = (1 - v^2/c^2)^{-1/2}$  and  $c$  is the speed of light. The relativistic adiabatic invariants are defined as

$$\mu = \int \gamma v_{\perp} dl = \int \frac{\gamma^2 v_{\perp}^2}{B} dt, \quad (2)$$

$$J = \int \gamma v_{\parallel} ds, \text{ and} \quad (3)$$

$$\Psi = \int \mathbf{B} \cdot d\mathbf{S}. \quad (4)$$

The integrations are taken along the gyromotion for  $\mu$ , along the bounce motion for  $J$ , and over a surface enclosed by the toroidal drift motion for  $\Psi$ .

In the following calculations, we assume  $\mathbf{E} = 0$ . As an external magnetic field  $\mathbf{B}$ , we use a pure dipole magnetic field generated by the superconducting (SC) magnet of RT-1 [10], as a typical magnetospheric dipole experiment. The rated current of the SC coil of RT-1 is 250 kAT (116A  $\times$  2160 turns) and the radius of the current center is 25 cm. The magnetic field lines, field strength, and typical examples of periodic and irregular particle motions are shown in Fig. 1. Here the toroidal rotation of the particle is due to the  $\nabla B$  and curvature drifts. Convergence of numerical calculations on the orbit and many particle behavior is checked in Appendix.

Figure 2 shows the typical temporal evolutions of the adiabatic invariants of a positron with periodic, quasiperiodic, and chaotic motions. The positrons were injected from  $r = 80$  cm on the equator ( $z = 0$  cm) plane with a pitch angle  $\theta$ , the angle between the field line, and the initial injection direction, satisfying  $\sin \theta = 0.5$ . Typical frequencies of the gyromotion, bounce motion, and toroidal rotation when  $E_k = 20$  keV are on the order of 100, 10, and 1 MHz, respectively. As shown in Fig. 2(3),  $\Psi$  is a good conserved quantity in all of the cases, indicating that the guiding center of the particle was generally on the initial magnetic surface. This is because the conservation of  $P_{\theta} \sim \Psi$  is realized due to the toroidal symmetry of the system independently of  $E_k$ . In the figure, we plotted  $\psi = 2\pi r_{z=0} A_{\theta}$ , where  $r_{z=0}$  is the radial position of the particle guiding center when it intersects the  $z = 0$  plane, and  $A_{\theta}$  is the  $\theta$  component of the magnetic vector potential at the particle position. In contrast,  $\mu$  and  $J$  are conserved only when  $E_k$  is small and positrons are magnetized. While they are good conserved quantities when  $E_k = 1$  keV, they have small variations at  $E_k = 20$  keV. When  $E_k = 100$  keV,  $\mu$  and  $J$  oscillate irregularly and are not conserved. There is a strong correlation

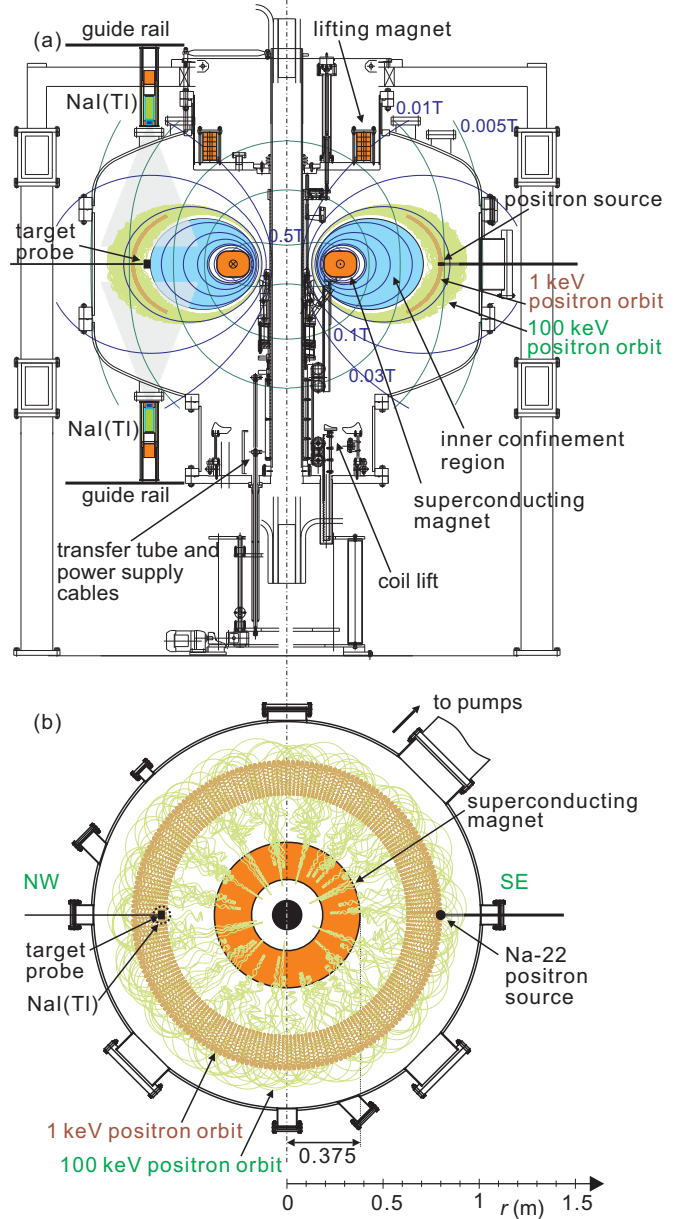


FIG. 1. (a) The poloidal cross section and (b) top view of RT-1. Thin lines in (a) show lines of force and strength of a magnetic field generated by a superconducting dipole field magnet. Projections of typical orbits of 1-keV and 100-keV positrons are plotted.

between  $\mu$  and  $J$ , indicating coupling between the gyro and bounce motions. In this case, the particle orbit is not integrable, as the two degrees of freedom leads to a chaotic motion.

The radial position of a positron and its frequency power spectrum are shown in Fig. 2 (4 and 5). When  $E_k = 1$  keV, as shown in Fig. 2(a), the radial position shows a periodic oscillation due to the gyromotion. Because of the inhomogeneous dipole field strength, a peak corresponding to the gyromotion has a broad nature centered approximately at 300 MHz in the frequency power spectrum. In this spectrum, rather sharp peaks for the bounce motions are found to be on the order of 10 MHz, located apart from the peak of gyromotions. When  $E_k = 20$  keV, as shown in Fig. 2(b), there is an overlap between

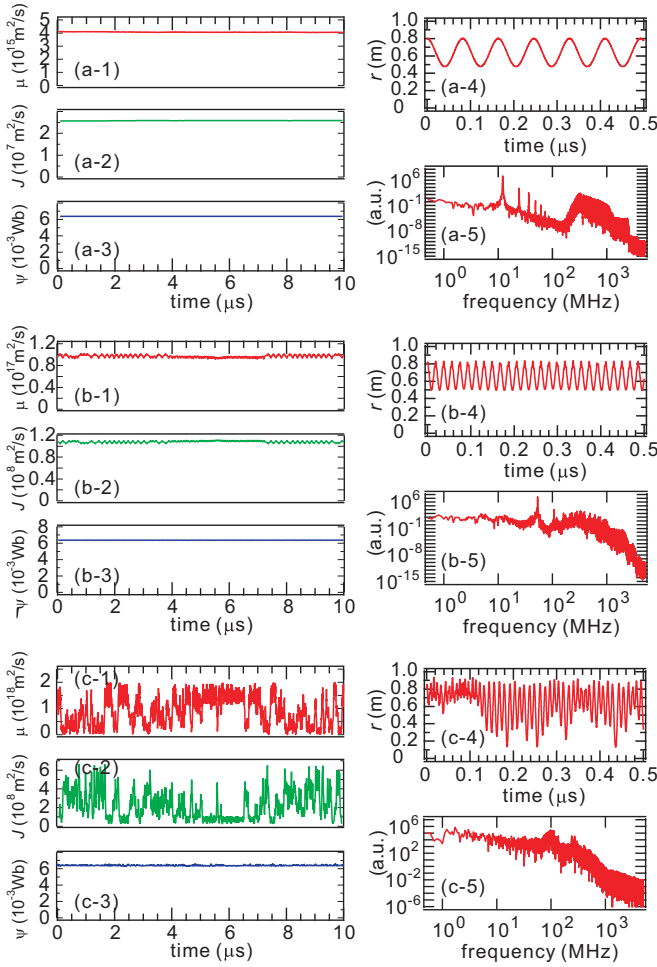


FIG. 2. Temporal variation of (1) magnetic moment  $\mu$ , (2) longitudinal invariant  $J$ , and (3) magnetic flux  $\Psi$ , (4) radial position of a positron, and (5) its frequency power spectrum. Positrons were injected from  $r = 80$  cm and  $z = 0$  cm with kinetic energy of (a)  $E_k = 1$  keV, (b) 20 keV, and (c) 100 keV.

the frequency ranges of gyro and bounce motions. The radial motion has a fluctuation component in addition to the periodic motion in this case. When  $E_k = 100$  keV in Fig. 2(c), the periodicity is almost completely lost.

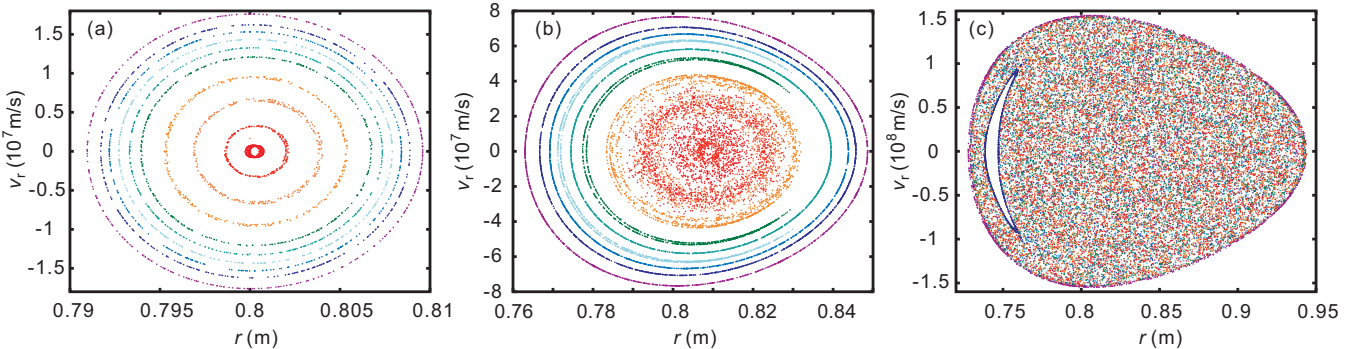


FIG. 3. The Poincaré maps of positron orbits in the dipole field of RT-1 injected from  $r = 80$  cm and  $z = 0$  cm with a kinetic energy of (a)  $E_k = 1$  keV, (b) 20 keV, and (c) 100 keV. The orbits were traced for  $50 \mu$ s, and 11 orbits with different initial pitch angles ( $\sin \theta = 0.1n$ ,  $0 \leq n \leq 10$ ) are superposed in each of the panels.

We observe the appearance of chaotic behavior of positron orbits using the Poincaré map. Figure 3 plots the intersections of the positron orbits with the surface of  $z = 0$  m ( $v_z > 0$ ) on the two-dimensional  $r$ - $v_r$  plane. In the low-energy case of  $E_k = 1$  keV, the plotted points lie on closed curves, indicating periodic or quasiperiodic behavior of the orbits. In the higher-energy case of  $E_k = 20$  keV, the closed curves are modulated and broken for the small  $\sin \theta$  cases. When  $E_k = 100$  keV, the plots fill a finite region. In this case, the periodicity of the orbit is lost and positrons have chaotic motions.

Whether the orbit is periodic or chaotic depends on both kinetic energy  $E_k$  and pitch angle  $\theta$  of positrons [32]. Figure 4 plots the numerical results on the conservation of  $\mu$  for various  $E_k$  and  $\theta$ . Here we judged that  $\mu$  was conserved for the cases like Fig. 2(a-1) and not conserved for the cases like Fig. 2(c-1). Orbits of particles with smaller pitch angles are chaotic at lower kinetic energies. This is because such particles travel toward stronger field regions compared with those with larger pitch angles, before being mirror reflected. This leads to the breakdown of adiabaticity at lower kinetic energies in stronger nonuniformity of the field strength. When injected from the edge confinement region of a dipole field generated by the SC coil of RT-1, the orbits can be chaotic when  $E_k$  exceeds approximately 10 keV. Because the energy distribution of positrons from a  $^{22}\text{Na}$  source has a broad peak above this value [Fig. 5(b-2)], it is possible that a considerable ratio of positrons has chaotic and long orbits in the confinement region.

## B. Flight length and flight time of positrons

In order to calculate the flight time and flight length of injected positrons, we traced the orbits of many positrons with  $E_k$  in the dipole field generated by the SC coil of RT-1. As a loss channel of positrons, we assumed a spherical structure of a radioactive source with a radius  $r_{\text{source}}$  centered at  $r = 80$  cm and  $z = 0$  cm. Here we supposed that the source is mechanically supported using thin wires that are negligibly smaller than the source size. We judged that a positron was lost and stopped calculation when the injected positron returned to the source region. In order to exclude unmagnetized positrons that are not trapped in a dipole field, we also assumed an outer wall at  $r = 2$  m. Because the field strength near the SC coil is stronger than 0.5 T and the Larmor radius of a

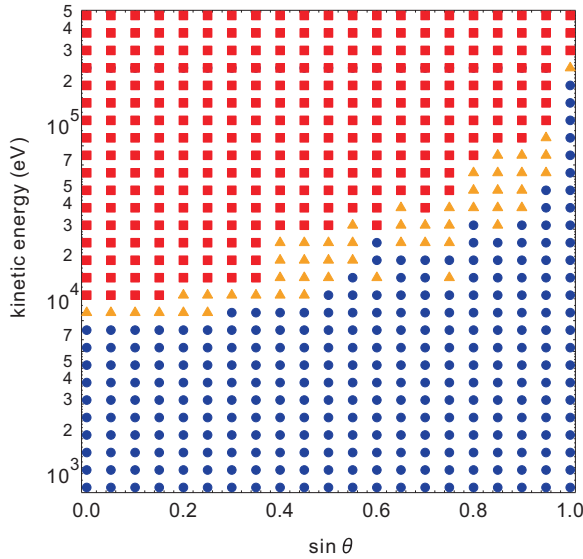


FIG. 4. (a) A conservation map of  $\mu$  for different kinetic energy and pitch angle of a positron injected from the edge confinement region at  $r = 80$  cm and  $z = 0$  cm. Circles are when  $\mu$  is conserved and positron motions are periodic. Squares are when  $\mu$  is not conserved and positron motions are chaotic. Triangles are marginal cases, as shown in Fig. 2(b).

500-keV positron is smaller than 6 mm, the SC coil case structure was not a loss channel for positrons [see Fig. 1(a)]. In the following calculations, we injected 26 555 positrons spatially isotropically from  $r = 80$  cm and  $z = 0$  cm.

Figure 5(a) shows the fraction of confined positrons as a function of flight length before hitting the source or the outer wall when  $r_{\text{source}} = 5$  cm. When  $E_k = 1$  keV and the orbit is periodic, positrons are immediately lost after short gyro and bounce motions, without filling the confinement region. As shown by the solid line in the figure, the flight lengths of particles are comparable to or below the typical length of the device size ( $\sim 1$  m). In the case of  $E_k = 20$  keV, there is a population of positrons with longer orbit lengths. The decay curve (the dashed line in the figure) clearly shows a steplike decrease because of the following reasons. Some positrons are lost (1 in the figure) during initial gyromotions and (2) after one bounce motion by hitting the source. The other particles make (3) single or (4) multiple toroidal precession motions before annihilation. At  $E_k = 100$  keV, as shown with the chain line, where most of particle orbits are chaotic, the ratio of positrons with long flight lengths drastically increased. The maximum flight length reached 1km, which is much longer than the device scale length. Figure 5(b-1) shows the averaged flight lengths of 26 555 positrons for different  $E_k$ . Above  $E_k = 3$  keV, some positrons have large Larmor radii and can toroidally circulate for a relatively long time before the recombination at the source. The chaotic effects further elongate the confinement time above approximately  $E_k = 20$  keV. The decrease of the averaged flight length at  $E_k = 500$  keV is caused by the enhanced loss of unmagnetized high-energy positrons at the outer wall. When compared with the energy distribution function of positrons emitted from  $^{22}\text{Na}$ , shown in Fig. 5(b-2), a considerable ratio of emitted

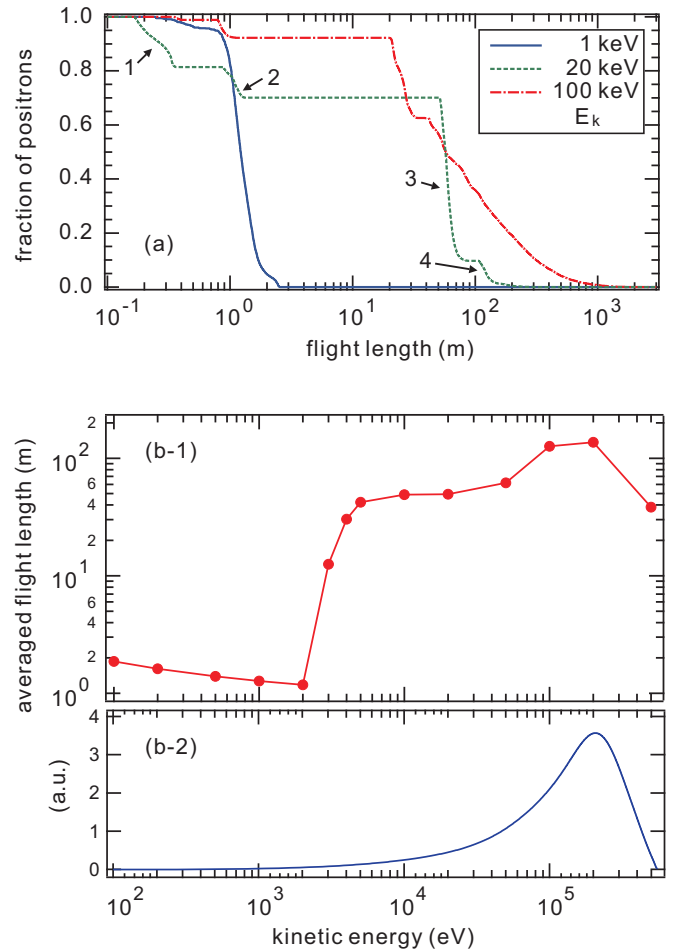


FIG. 5. (a) Fraction of confined positrons as a function of flight length for three different  $E_k$ . (b-1) Averaged flight lengths as a function of  $E_k$ . The radius of the source was  $r_{\text{source}} = 5$  cm. (b-2) An emission spectrum of positrons from  $^{22}\text{Na}$  is shown for comparison.

positrons has orbit lengths that are much longer than the device scale length.

The flight length and flight time of course strongly depend also on the source size. Figure 6(a) shows the fraction of flying positrons with  $E_k = 100$  keV for different source radius  $r_{\text{source}}$ . When  $r_{\text{source}}$  is below 2 cm, most of positrons have much longer flight times than the device size. Some particles flew longer than 100 km, and the averaged flight length reached 10 km at  $r_{\text{source}} = 0.5$  cm, although, experimentally, it is not straightforward to realize such a small source structure. As shown in Fig. 6(b), the averaged flight length shows an almost linear dependence on the cross-sectional area of the source, indicating that positrons distributed homogeneously in the confinement region and returned to the source region randomly.

Figure 7 plots the flight time and flight length of positrons emitted from a  $^{22}\text{Na}$  source, calculated including the effects of the broad energy distribution. In these calculations, 15 180 positrons of up to  $E_k = 540$  keV were injected spatially isotropically from  $r = 80$  cm and  $z = 0$  cm. We discretized the distribution function shown in Fig. 5(b-2) and used these data as a weighting factor for the calculation of the fraction of

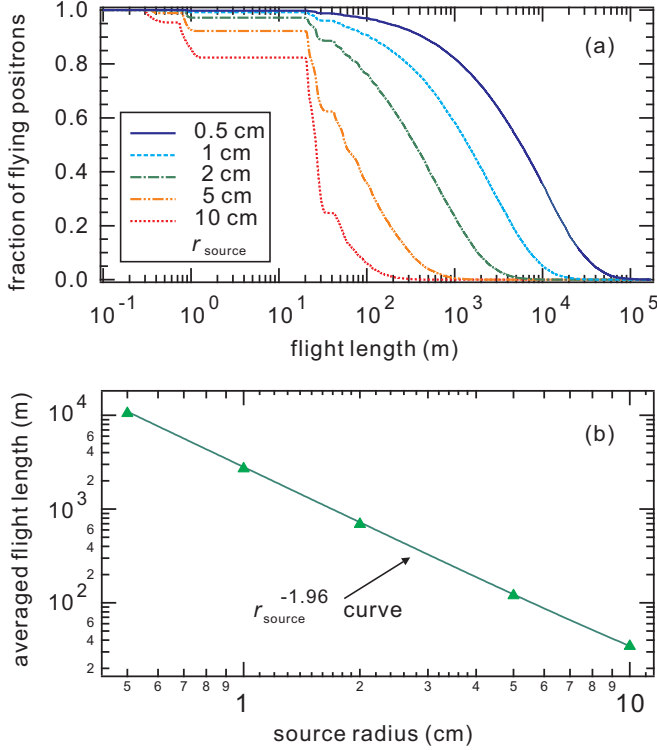


FIG. 6. (a) Fraction of monoenergetic positrons spatially isotropically injected with  $E_k = 100$  keV as functions of flight length for different source size  $r_{\text{source}}$ . (b) The averaged flight length of positrons as a function of  $r_{\text{source}}$ . The best power-law fitting was obtained for  $\propto r_{\text{source}}^{-1.96}$ .

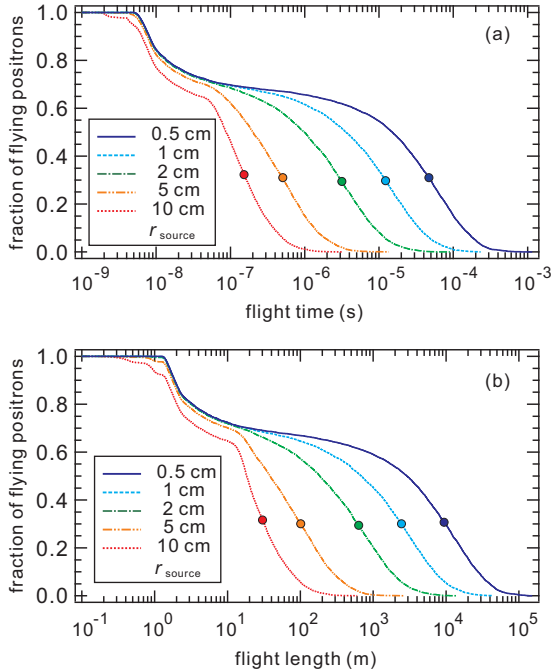


FIG. 7. Fraction of positrons injected from a  $^{22}\text{Na}$  source spatially isotropically, as functions of (a) flight time and (b) flight length for different  $r_{\text{source}}$ . Circles show averaged values of flight times and lengths for all particles.

flying positrons. Among emitted positrons, those with periodic motions go back to the source and are lost in short time scales. However, a substantial ratio of positrons have chaotic and long orbits. These positrons circulate toroidally many times, filling the confinement region. It results in the steady formation of a hollow toroidal positron cloud in the outer confinement region, as shown in Fig. 1(a). For a rather optimistic value of  $r_{\text{source}} = 0.5$  cm, the averaged confinement time of positrons is  $4.7 \times 10^{-5}$  s (Fig. 7).

By using a commercially available 100-mCi (3.7-GBq)  $^{22}\text{Na}$  source in a clean ultrahigh vacuum (UHV) environment, it is expected that a hollow toroidal positron cloud with  $N_0 \sim 1 \times 10^4$  particles is steadily generated in the outer confinement region. Because positron trajectories are confined in a volume of  $\sim 0.3$  m<sup>3</sup>, the averaged positron density in this region is  $n_0 \sim 3 \times 10^5$  m<sup>-3</sup>. The dipole magnetic field has strong inward diffusion effects toward the strong-field region [9]. Therefore, once such a hollow positron cloud is generated steadily, effective radial transport leads to the formation of a dense positron cloud in the inner confinement region. The particle balance in the inner confinement region is given by

$$\frac{dN_1}{dt} = \int \Gamma dS - \frac{N_1}{\tau}, \quad (5)$$

where  $N_1$  and  $\tau$  are the total positron number and the particle confinement time in the inner confinement region.  $\Gamma$  is the particle flux from the outer region to the inner region. We estimate the confinement time in the inner region  $\tau$  from the previous experiments in RT-1, where pure electron plasmas were stably trapped for more than 300 s [11]. Here we use  $\tau = 10^3$  s, assuming an improved vacuum condition compared to RT-1. When appropriate low-frequency fluctuations are applied at the edge region so an inward particle transport of  $\int \Gamma dS = 10^7$  s<sup>-1</sup> is realized (i.e., approximately 1% of positrons from a 1-GBq source are transported inward),  $N_1$  on the order of  $10^{10}$  is expected in a steady state.

The design of slow electrostatic fluctuations suitable for the efficient inward diffusion of high-energy positrons from a  $^{22}\text{Na}$  source and their experimental verification remain to be done as future studies. Although relatively long orbits were realized by the chaos effects, the isotope source structure was still a serious loss channel of positrons. Such a high loss rate will be greatly reduced by transporting positrons into a strong-field region, as observed in electron plasma experiments in RT-1 [7, 11]. On the formation of positron plasmas, a limit of particle accumulation set by interactions with remaining neutrals should be considered. By choosing appropriate plasma parameters in a UHV environment, lifetimes decided by several processes [36, 37] are much longer than the trapping times of positrons discussed here.

It is also noted that, when one further intends to confine positrons as a plasma, i.e., satisfying a condition that the Debye length is much smaller than the system size, another challenging thing is the cooling of high-energy positrons. Especially near the SC dipole field coil, positrons emitted primarily perpendicular to the field lines are expected to be cooled by the synchrotron radiation. However, the synchrotron cooling time [38] is  $\tau_D \sim 3\pi\epsilon_0 m_e c^3 / e^2 \omega_{ec}^2 \sim 10$  s at  $B = 0.5$  T, a typical field strength near the SC coil of RT-1. This is not sufficient to cool high-energy positrons from a  $^{22}\text{Na}$

source. Further optimizations are also needed on this topic as future studies.

### III. POSITRON INJECTION INTO RT-1

In order to experimentally demonstrate the chaotic long orbits of high-energy positrons in the dipole configuration, and also to verify the accuracy of the numerical calculations, we injected positrons into the dipole field of RT-1 using a 1-MBq (27- $\mu$ Ci)  $^{22}\text{Na}$  source [39]. Here we report the results and compare them with numerical calculations. The RT-1 device (Fig. 1) is a “laboratory magnetosphere” constructed for the studies of high-temperature fusion plasmas [5] suitable for burning advanced fuels [1], as well as for the investigation of toroidal non-neutral plasmas [7,11] including antimatters. Inside the vacuum chamber, RT-1 has a Bi-2223 high-temperature superconducting dipole field magnet [10]. The magnet can be levitated using a feedback-controlled lifting magnet system located at the top of the chamber, in order to minimize perturbations to the plasma. In the present experiment, however, the superconducting magnet was mechanically supported, and positrons were injected into a pure dipole field configuration. The rated current value of the magnet is 250 kAT. The vacuum chamber is 2 m in diameter and the base pressure was  $7 \times 10^{-7}$  Pa. More detailed explanations of RT-1 can be found in Ref. [10].

As shown in Fig. 1, positrons were injected from a sealed 1-MBq  $^{22}\text{Na}$  source ( $\phi$ 19.1 mm in diameter and 0.65 mm in thickness) positioned at the edge of a movable thin supporting rod at the southeast (SE) port. The source and the supporting rod were electrically connected to the vacuum chamber. Positrons were detected by observing annihilation  $\gamma$  rays using two NaI(Tl) scintillator detectors (Scionix type 25B25/1.5 scintillators with Ortec type 276 photomultipliers) viewing a  $10 \times 10 \times 1$  mm stainless steel target plate located at the edge of a supporting rod at the northwest (NW) port. The detectors were mounted on radially movable guide rails and had the maximum detection sensitivity at the position of view ports at  $r_{\text{detector}} = 72$  cm, as shown in the figure. The detector positions were aligned by conducting coincidence measurements of  $\gamma$  rays by placing the  $^{22}\text{Na}$  source at the movable target plate. We calibrated the detectors and decided the counting efficiency of the coincidence measurements at the target plate also by using this method. For the magnetic shielding, the photomultipliers were covered with electromagnetic soft iron tubes with a thickness of 1 cm. The signals were processed with Ortec 855 amplifiers and Amptek PX4 multichannel analyzers. For coincidence counting, the signals from the amplifiers were sent to Ortec type 551 timing single channel analyzers and a type 418A coincidence unit.

Figure 8(a) shows a  $\gamma$ -ray energy spectrum, which indicates the trapping and toroidal circulation of positrons in the dipole field. The  $^{22}\text{Na}$  source was located at  $r_{\text{source}} = 80$  cm at the SE port. The  $\gamma$  rays were observed by the detector located at  $r_{\text{detector}} = 72$  cm at the top of the chamber viewing the target plate at  $r_{\text{target}} = 72$  cm, and both of them were located at NW ports, as shown in Fig. 1. The 511-keV peak is the annihilation signal of positrons at the target plate. Another small peak at 1.27 MeV corresponds to transition  $\gamma$  rays from the  $^{22}\text{Na}$  source. Because the detector did not exclusively

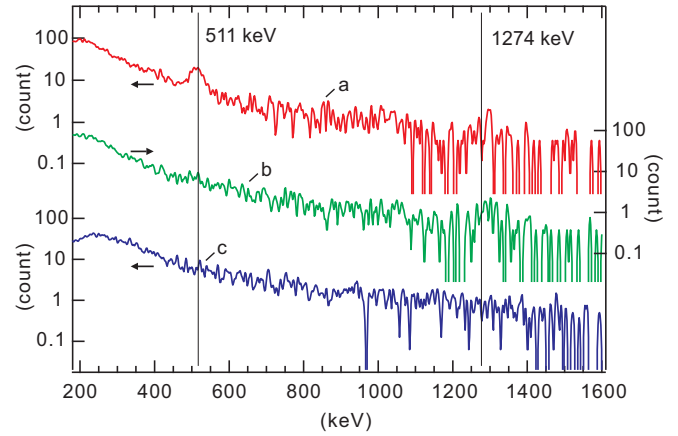


FIG. 8. Annihilation  $\gamma$ -ray energy spectra recorded for 1200 s (a) when the target plate was located at  $r_{\text{target}} = 72$  cm, (b) when the target plate was located at outside the chamber, and (c) when the dipole field magnet was turned off while  $r_{\text{target}} = 72$  cm. The  $^{22}\text{Na}$  source was positioned at  $r_{\text{source}} = 80$  cm (Fig. 1) for all of the cases.

view the position of the target plate, it is useful to compare the signals with different experimental conditions. As shown in the figure, a 511-keV peak was not observed [Fig. 8(b)] when the target plate was removed from the vacuum chamber ( $r_{\text{target}} = 105$  cm) and [Fig. 8(c)] when the dipole magnetic field was turned off while keeping the target plate inside the chamber at  $r_{\text{target}} = 72$  cm. Therefore we interpret the 511 keV  $\gamma$  signal, observed in Fig. 8(a), as annihilation signals of positrons which were injected from the source, trapped in the dipole magnetic field, and hit the target after at least a  $180^\circ$  toroidal rotation. These results clearly show the existence of long-lived positrons with chaotic motions in the geometry of RT-1, which were not immediately lost at the source.

Figure 9 plots the counts of 511-keV  $\gamma$  rays for the various  $r_{\text{target}}$  values measured with the detector at  $r_{\text{detector}} = 72$  cm at the top of the chamber. The  $^{22}\text{Na}$  source was again located at  $r_{\text{source}} = 80$  cm at the SE port. Here the edge of the dipole field coil is at 37.5 cm and the chamber wall is located at  $r = 100$  cm. As the target plate was mechanically supported by a thin rod, a small but non-negligible ratio of positrons annihilated on this supporting rod. In order to eliminate these

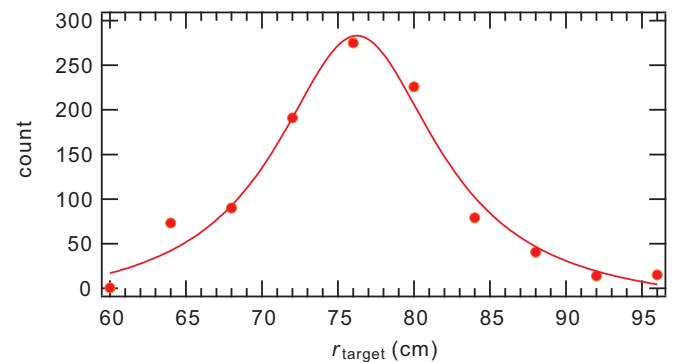


FIG. 9. Counts of annihilation 511-keV  $\gamma$  rays from the target plate as a function of  $r_{\text{target}}$ . Counts from the supporting rod of the target were subtracted. Positrons were injected from  $r_{\text{source}} = 80$  cm at the SE port. The detector was located at  $r_{\text{detector}} = 72$  cm using the NW port. The thin line is a guide to the eye.

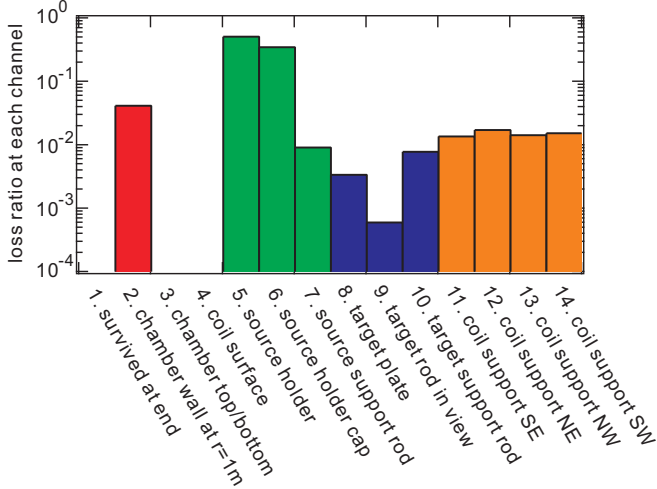


FIG. 10. Typical calculated example of the ratio of positrons lost at each of the channels. The  $^{22}\text{Na}$  source and the target plate were located at  $r_{\text{source}} = r_{\text{target}} = 72$  cm.

effects and to count annihilation  $\gamma$  rays mainly from the target plate, the plotted data were obtained by subtracting the counts measured by inserting the supporting rod without attaching the target plate, which were used as offset data. The results indicate that positrons were distributed between a radial position of approximately 65 to 90 cm. The observed radial spread of the profile is comparable to the Larmor radius  $r_L = \gamma m v_{\perp} / eB = 11$  cm for a 100-keV positron at the source position.

Although the above measurements suggest that positrons were trapped in a spatially finite region, as predicted by the orbit calculations, it is not straightforward to quantitatively compare these experimental data with numerical results. This is because the ratio of positrons lost at the target and other loss channels depends on  $r_{\text{target}}$ . Therefore, the above measurements include the effects of annihilation signals from the loss channels other than the target plate. Also, the  $\gamma$ -ray transmission rate through the view port and the chamber wall, as well as the solid angle subtended by the detector, is not constant for different  $r_{\text{target}}$  when observed with the scintillation detector fixed at  $r_{\text{detector}} = 72$  cm. As shown in Fig. 1(a), the vignetting effects of the observation port result in the decrease of counts when the radial position of the target is not very close to  $r = 72$  cm. In order to solve this problem, we conducted coincidence measurements of the annihilation  $\gamma$  rays as a function of  $r_{\text{source}}$  by fixing both the target and two detectors at  $r_{\text{target}} = r_{\text{detector}} = 72$  cm and compared the data with orbit calculations.

Figure 10 shows the numerical results of typical loss channels of positrons in the supported experiments in RT-1. We again traced trajectories of 15 180 particles injected from  $r_{\text{source}} = 72$  cm at the SE port, satisfying the energy distribution of positrons from a  $^{22}\text{Na}$  source. As the loss channels, we considered the chamber walls (2 and 3 in the figure), the SC coil surface (4), the source structures (5–7), the target structures (8–10), and the coil support structures (11–14). In the present conditions, most of positrons were lost at the source itself and the source holder parts. One of the reasons for such a high loss rate at the source is the structure of the source holder, which will be easily improved in future experiments;

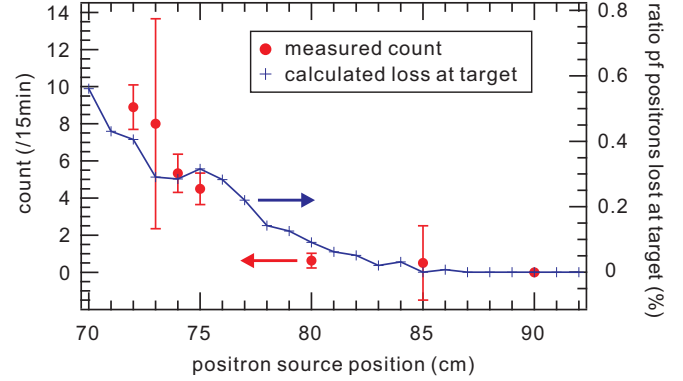


FIG. 11. Comparison of coincidence counts of annihilation  $\gamma$  rays and numerical results of the ratio of positrons lost at the target plate and the target supporting rod inside the view of detectors. The target plate and the detectors were located at  $r_{\text{target}} = r_{\text{detector}} = 72$  cm.

because the present planer source holder was open only for one direction, at least 50% of positrons were immediately lost after injection. Because the SC coil was supported, the coil supporting structures were also considerable loss channels. Some high-energy positrons with large Larmor radii were lost by hitting the chamber wall. The other part of positrons circulated toroidally and reached the target plate and its supporting structures.

The results of the coincidence measurements and calculations are shown in Fig. 11. The circles show the coincidence counts measured with the detectors viewing the target plate at  $r = r_{\text{target}} = r_{\text{detector}} = 72$  cm for various source positions. The thin line in the figure shows the calculation data, the ratio of positrons that were lost on the target plate for each value of  $r_{\text{source}}$ . Here we summed the ratio of positrons lost at the target plate and at the target support rod inside the view of the two detectors (channels 8 and 9 in Fig. 10). The count rate can be compared with the ratio of positrons annihilated at the target. According to the calibration with the 1-MBq  $^{22}\text{Na}$  source, one coincidence count in Fig. 11 corresponded to the loss of 0.056% of the injected positrons from the source, as scaled in the figure. In spite of the rather complicated geometries, the coincidence counts and the loss rate at the target showed a fairly good agreement. The remaining disagreement would be attributed to a small position error of the target plate at the calibration and at the injection experiments. These results give a strong support on the validity of the numerical results on the chaotic behavior of positrons presented in Sec. III.

#### IV. SUMMARY

Numerical analysis of orbits showed that a considerable ratio of positrons emitted from a  $^{22}\text{Na}$  source have chaotic long orbits in a magnetospheric dipole field configuration, which is realized due to the breakdown of the conservation of  $\mu$  and  $J$ . It is noted that this is in marked contrast to the case of magnetized plasmas consisting of low energy charged particles, where breakdown of  $\Psi$  plays an important role in the self-organization process [2]. The chaotic behavior of the particle orbit results in long flight paths of positrons before annihilation, which enables spontaneous formation of a

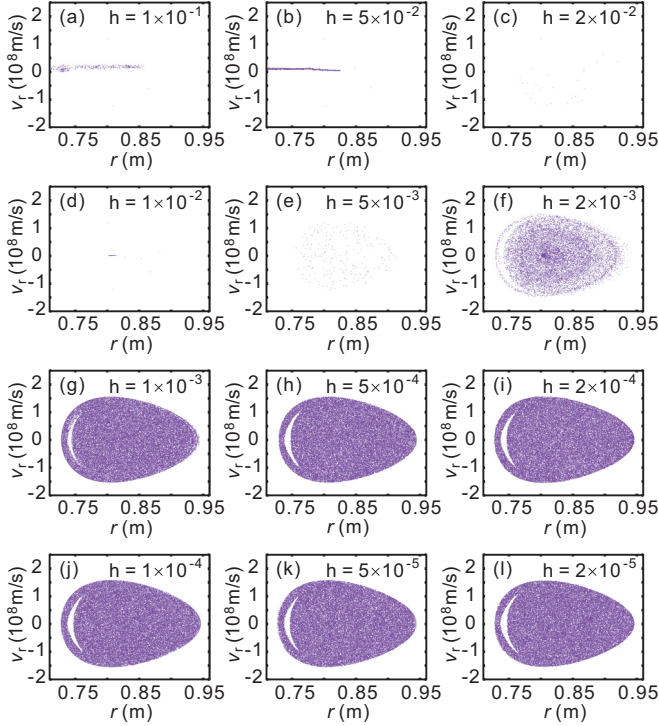


FIG. 12. The Poincaré maps of a positron of  $E_k = 100$  keV for a different time step  $h$ . The calculation conditions are same as the case of Fig. 3(c) and  $\sin \theta = 0.5$ .

toroidal hollow positron cloud in the edge confinement region of the dipole field.

Experiments with a small  $^{22}\text{Na}$  source in RT-1 demonstrated that a part of energetic positrons performed toroidal circulation and filled a finite confinement region before annihilation. We confirmed that the experimental observations are consistent with numerical analysis on the loss channels of positrons in the experimental configuration of RT-1.

It is noted that, as future studies, the present results are potentially applicable to the formation of a dense positron cloud in a dipole field. In a strongly inhomogeneous dipole field, it is known that slow fluctuations drive inward diffusion of particles toward the strong-field region. When optimized fluctuating electric fields are applied to the hollow positron cloud, efficient inward transport of positrons toward the strong-field region of a levitated dipole is expected.

#### ACKNOWLEDGMENTS

T.S.P., H.S., and J.S. thank the PAX/APEX team of IPP for comments and suggestions. This work was partially supported by JSPS KAKENHI Grant No. 25707043.

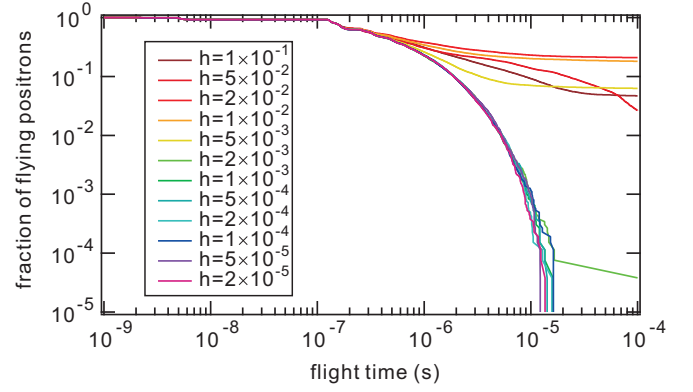


FIG. 13. Calculation results on fraction of injected positrons for a different time step  $h$ , normalized by the inverse of the typical cyclotron frequency of positrons. The calculation conditions are same as the case of  $r_{\text{source}} = 5$  cm in Fig. 6(a).

#### APPENDIX: CONVERGENCE OF ORBIT CALCULATIONS

In the presence of round-off errors in iterative calculations, numerical integration of the equation of motion is not always a good approximation of a true trajectory. This can be a serious problem, especially for a chaotic system, where a strong sensitivity of solutions to initial data is the key signature. However, such numerical calculations are not meaningless, because the shadowing lemma predicts the existence of a true orbit within a finite region near the numerically obtained pseudo-orbits in many systems [40–42]. When the noisy pseudo-orbits are close to the true orbit, statistical calculation of chaotic orbits for many particles may converge into a good approximation of the behavior of a true system. Here we check the convergence of the calculations conducted in this study.

Figure 12 shows the Poincaré maps of the positron orbit in RT-1 for a different time step  $h$  of integration, which is normalized by the typical positron cyclotron period of  $10^{-9}$  s in RT-1. We found that the area that filled with intersection points of the orbits is independent of  $h$  typically below  $h = 5 \times 10^{-4}$ , indicating that the numerical integration reached convergence and the calculated orbits shadow a certain orbit. For many particle calculations, Fig. 13 shows temporal evolutions of the fraction of confined positrons before hitting and lost at a source of a radius  $r_{\text{source}} = 5$  cm for various  $h$  values. As shown in the figure, we confirmed that the many particle calculations conducted in this study converged into a solution with fluctuating errors on the order of 0.01% when  $h$  was below approximately  $2 \times 10^{-3}$  for the wide range of  $E_k$  of positrons emitted from the  $^{22}\text{Na}$  source.

- [1] A. Hasegawa, *Comments Plasma Phys. Control. Fusion* **11**, 147 (1987).
- [2] Z. Yoshida, H. Saitoh, Y. Yano, H. Mikami, N. Kasaoka, W. Sakamoto, J. Morikawa, M. Furukawa, and S. M. Mahajan, *Plasma Phys. Control. Fusion* **55**, 014018 (2013).

- [3] M. Schulz and L. J. Lanzerotti, *Particle Diffusion in the Radiation Belts* (Springer, New York, 1974).
- [4] H. P. Warren and M. E. Mauel, *Phys. Rev. Lett.* **74**, 1351 (1995).
- [5] M. Nishiura, Z. Yoshida, H. Saitoh, Y. Yano, Y. Kawazura, T. Nogami, M. Yamasaki, T. Mushiake, and A. Kashyap, *Nucl. Fusion* **55**, 053019 (2015).

- [6] A. C. Boxer, R. Bergmann, J. L. Ellsworth, D. T. Garnier, J. Kesner, M. E. Mauel, and P. Woskov, *Nat. Phys.* **6**, 207 (2010).
- [7] Z. Yoshida, H. Saitoh, J. Morikawa, Y. Yano, S. Watanabe, and Y. Ogawa, *Phys. Rev. Lett.* **104**, 235004 (2010).
- [8] Y. Kawazura, Z. Yoshida, M. Nishiura, H. Saitoh, Y. Yano, T. Nogami, N. Sato, M. Yamasaki, A. Kashyap, and T. Mushiake, *Phys. Plasmas* **22**, 112503 (2015).
- [9] Z. Yoshida and S. M. Mahajan, *Prog. Theor. Exp. Phys.* (2014) 073J01.
- [10] Y. Ogawa, Z. Yoshida, J. Morikawa, H. Saitoh, S. Watanabe, Y. Yano, S. Mizumaki, and T. Tosaka, *Plasma Fusion Res.* **4**, 020 (2009).
- [11] H. Saitoh, Z. Yoshida, J. Morikawa, Y. Yano, H. Hayashi, T. Mizushima, Y. Kawai, M. Kobayashi, and H. Mikami, *Phys. Plasmas* **17**, 112111 (2010).
- [12] J. D. Daugherty, J. E. Eninger, and G. S. Janes, *Phys. Fluids* **12**, 2677 (1969).
- [13] P. Zaveri, P. I. John, K. Avinash, and P. K. Kaw, *Phys. Rev. Lett.* **68**, 3295 (1992).
- [14] H. Himura, H. Wakabayashi, Y. Yamamoto, M. Isobe, S. Okamura, K. Matsuoka, A. Sanpei, and S. Masamune, *Phys. Plasmas* **14**, 022507 (2007).
- [15] J. P. Kremer, T. S. Pedersen, R. G. Lefrancois, and Q. Marksteiner, *Phys. Rev. Lett.* **97**, 095003 (2006).
- [16] S. Pahari, H. S. Ramachandran, and P. I. John, *Phys. Plasmas* **13**, 092111 (2006).
- [17] J. P. Marler and M. R. Stoneking, *Phys. Rev. Lett.* **100**, 155001 (2008).
- [18] Z. Yoshida, Y. Ogawa, J. Morikawa, H. Himura, S. Kondoh, C. Nakashima, S. Kakuno, M. Iqbal, F. Volponi, N. Shibayama, and S. Tahara, *AIP Conf. Proc.* **498**, 397 (1999).
- [19] T. Sunn Pedersen, J. R. Danielson, C. Hugenschmidt, G. Marx, X. Sarasola, F. Schauer, L. Schweikhard, C. M. Surko, and E. Winkler, *New J. Phys.* **14**, 035010 (2012).
- [20] H. Saitoh, J. Stanja, E. V. Stenson, U. Hergenbahn, H. Niemann, T. Sunn Pedersen, M. R. Stoneking, C. Piochacz, and C. Hugenschmidt, *New J. Phys.* **17**, 103038 (2015).
- [21] J. Stanja, U. Hergenbahn, H. Niemann, N. Paschkowski, T. Sunn Pedersen, H. Saitoh, E. V. Stenson, M. R. Stoneking, C. Hugenschmidt, and C. Piochacz, *Nucl. Instr. Methods A* **827**, 52 (2016).
- [22] V. Tsytovich and C. B. Wharton, *Comments Plasma Phys. Controlled Fusion* **4**, 91 (1978).
- [23] N. Iwamoto, *Phys. Rev. E* **47**, 604 (1993).
- [24] P. Helander, *Phys. Rev. Lett.* **113**, 135003 (2014).
- [25] R. G. Greaves and C. M. Surko, *Phys. Rev. Lett.* **75**, 3846 (1995).
- [26] W. Oohara and R. Hatakeyama, *Phys. Rev. Lett.* **91**, 205005 (2003).
- [27] G. Sarri, K. Poder, J. Cole, W. Schumaker, A. D. Piazza *et al.*, *Nat. Commun.* **6**, 6747 (2015).
- [28] C. Hugenschmidt, C. Piochacz, M. Reiner, and K. Schreckenbach, *New J. Phys.* **14**, 055027 (2012).
- [29] J. R. Danielson, D. H. E. Dubin, R. G. Greaves, and C. M. Surko, *Rev. Mod. Phys.* **87**, 247 (2015).
- [30] A. Hasegawa, *Phys. Scr.* **116**, 72 (2005).
- [31] A. J. Dragt and J. M. Finn, *J. Geophys. Res.* **81**, 2327 (1976).
- [32] S. Murakami, T. Sato, and A. Hasegawa, *Phys. Fluids B* **2**, 715 (1990).
- [33] Z. Yoshida, H. Asakura, H. Kakuno, J. Morikawa, K. Takemura, S. Takizawa, and T. Uchida, *Phys. Rev. Lett.* **81**, 2458 (1998).
- [34] C. Nakashima, Z. Yoshida, H. Himura, M. Fukao, J. Morikawa, and H. Saitoh, *Phys. Rev. E* **65**, 036409 (2002).
- [35] R. Numata and Z. Yoshida, *Phys. Rev. Lett.* **88**, 045003 (2002).
- [36] R. G. Greaves and C. M. Surko, *AIP Conf. Proc.* **606**, 10 (2002).
- [37] H. Saitoh, J. Stanja, E. V. Stenson, U. Hergenbahn, H. Niemann, T. S. Pedersen, M. R. Stoneking, C. Piochacz, and C. Hugenschmidt, *J. Phys.: Conf. Ser.* **505**, 012045 (2014).
- [38] B. R. Beck, J. Fajans, and J. H. Malmberga, *Phys. Plasmas* **3**, 1250 (1996).
- [39] H. Saitoh, Z. Yoshida, J. Morikawa, Y. Yano, N. Kasaoka, W. Sakamoto, and T. Nogami, *AIP Conf. Proc.* **1521**, 63 (2013).
- [40] R. Bowen, *J. Diff. Equations* **18**, 333 (1975).
- [41] C. Grebogi, S. M. Hammel, J. A. Yorke, and T. Sauer, *Phys. Rev. Lett.* **65**, 1527 (1990).
- [42] B. A. Coomes, H. Koçak, and K. J. Palmer, *J. Comput. Appl. Math.* **52**, 35 (1994).